TOPOLOGY OPTIMIZATION FOR FLUID FLOW PROBLEMS USING THE VIRTUAL ELEMENT METHOD

Miguel A. A. Suárez[a], Juan S. Romero[b] and Ivan F. M. Menezes[c]

[a]*Department of Mechanical Engineering, Pontifical Catholic University of Rio de Janeiro PUC-Rio, Rio de Janeiro, Brazil, miguel.ampueros@aluno.puc-rio.br, http://www.mec.puc-rio.br*

[b]*Department of Mechanical Engineering, Federal University of Espirito Santo UFES, Vitória , Brazil, juan.saenz@ufes.br, http://www.engenhariamecanica.ufes.br*

[c]*Department of Mechanical Engineering, Pontifical Catholic University of Rio de Janeiro PUC-Rio, Rio de Janeiro, Brazil, ivan@puc-rio.br, http://www.mec.puc-rio.br*

Keywords: Topology optimization, fluid flow problems, virtual element method, projection operators.

Abstract. This work presents some applications of topology optimization for fluid flow problems using the Virtual Element Method (VEM) (Veiga et al. 2013) in arbitrary two-dimensional domains. The idea is to design an optimal layout for the incompressible Newtonian fluid flow, governed by the Stokes equations, to minimize the viscous drag. The porosity approach proposed by (Borrvall and Petersson, 2003) is used in the topology optimization formulation. To solve the governing boundary value problem, the recently proposed VEM is used. The key feature that distinguishes the VEM from the classical finite element method is that the interpolation functions in the interior of the elements are not required to be computed explicitly. The use of appropriate local projection maps allows for the extractions of the rigid body motion and the constant strain components of the deformation. Therefore, the computation of the local matrices is reduced to the evaluation of geometric quantities on the boundaries of the elements. Finally, several numerical examples are provided to demonstrate the efficiency and applicability of the VEM for the topology optimization of fluid flow problems.

1   INTRODUCTION

The method of topology optimization for fluid flow problems first appeared in the literature in 2003. It was originally developed by (Borrvall and Petersson, 2003); examples for the optimal layout of channel flows with minimized drag or pressure drop are presented in his works. In the last decade, the method has been extended to other design objectives and constraints functions. Recently, the VEM has been successfully applied to a variety of problems, such as elasticity, heat, and fluid flow problems (e.g., Ahmad et al. (2013), Sutton (2017), Chi et al. (2017), and Brenner et al. (2017)) and is attractive in terms of computational efficiency compared to the FEM method.

The present paper aims to present some applications of topology optimization for fluid problems, specifically for incompressible and Newtonian fluids, using the VEM in arbitrary two-dimensional domains. It is organized as follows: In section 2, the theoretical background regarding Stokes–Darcy problem is briefly presented together with some theoretical background on the VEM. In section 3, we describe the topology optimization method applied to the fluid flow problem. In section 4, numerical examples are presented to demonstrate the effectiveness of the proposed method. Finally, concluding remarks are presented in section 5.

2   VIRTUAL ELEMENT METHOD (VEM)

2.1 Stokes–Darcy problem

The Stokes–Darcy equation, typically known as the Brinkman equation, is expressed as follows (Gartling et al. 2007):

$$\begin{cases} \mu \nabla^2 \boldsymbol{u} + \bar{\alpha}\boldsymbol{u} = \nabla p - \boldsymbol{f}, \\ \nabla.\boldsymbol{u} = 0 \end{cases} \tag{1}$$

where $\bar{\alpha}$ is the inverse permeability of the porous medium.

The Eq. (1) is typically used in topology optimization problems, where the parameter $\bar{\alpha}$ allows for the determination of the material type (solid/fluid) of a given point in the optimization domain.

The weak formulation of the problem is obtained from Eq. (1) using the weighted residual method (WRM), as shown in Eq. (2), where $\boldsymbol{v}$ and q are the velocity and pressure virtual weighting functions, respectively. Further, $(\boldsymbol{u}, p) \in V \times Q$ is to be obtained such that:

$$\begin{cases} a(\boldsymbol{u},\boldsymbol{v}) + a_\alpha(\boldsymbol{u},\boldsymbol{v}) + b(\boldsymbol{v},p) = l(\boldsymbol{v}), \quad \forall \boldsymbol{v} \in V \\ \qquad\qquad b(\boldsymbol{u},q) = 0, \qquad \forall q \in Q \end{cases}, \tag{2}$$

where, in turn, $a: V \times V \to \mathbb{R}, b: V \times Q \to \mathbb{R}, \boldsymbol{l}: V \to \mathbb{R}$ are the bilinear forms defined by

$$\begin{cases} a(\boldsymbol{u},\boldsymbol{v}) \coloneqq \mu \int_\Omega \nabla \boldsymbol{u}:\nabla \boldsymbol{v} \, d\Omega \,, a_\alpha(\boldsymbol{u},\boldsymbol{v}) \coloneqq \bar{\alpha} \int_\Omega \boldsymbol{u}.\boldsymbol{v} \, d\Omega \\ b(\boldsymbol{v},p) \coloneqq - \int_\Omega p(\nabla.\boldsymbol{v}) \, d\Omega \,, \ b(\boldsymbol{u},q) \coloneqq \int_\Omega q(\nabla.\boldsymbol{u}) \, d\Omega \end{cases}, \quad l(\boldsymbol{v}) \coloneqq - \int_\Omega \boldsymbol{f}.\boldsymbol{v} \, d\Omega, \tag{3}$$

Let $\{\phi_j\}_{j=1}^{N}$ be a basis of V_h and let $\{\psi_j\}_{j=1}^{M}$ be a basis of Q_h. If

$$\boldsymbol{u}_h = \sum_{j=1}^{N} \boldsymbol{u}_j \phi_j \quad , \quad p_h = \sum_{j=1}^{M} p_j \psi_j$$

then, it leads to the following linear systems of equations

$$\begin{cases} \displaystyle\sum_{j=1}^{N} \boldsymbol{u}_j a_h(\phi_i,\phi_j) + \sum_{j=1}^{N} \boldsymbol{u}_j a_h^{\alpha}(\phi_i,\phi_j) + \sum_{l=1}^{M} p_l b_h(\phi_i,\psi_l) = - \int_{\Omega} f_i \cdot \phi_j \, d\Omega \\[4mm] \displaystyle\sum_{j=1}^{N} \boldsymbol{u}_j b_h(\phi_j,\psi_l) + \lambda \int_{\Omega} q_h \, d\Omega = 0 \\[4mm] \displaystyle\int_{\Omega} p_h \, d\Omega = 0 \end{cases} \tag{4}$$

Or, equivalently

$$\boldsymbol{K}\boldsymbol{x} = \boldsymbol{F}, \tag{5}$$

where $\boldsymbol{x} = (\boldsymbol{u_1},\dots,\boldsymbol{u}_N, p_1,\dots, p_M, \lambda)^T$, $\{p_1,\dots,p_M\}$ are the element pressures, λ is the Lagrange multiplier,

$$\boldsymbol{K} = \begin{bmatrix} \boldsymbol{A} & \boldsymbol{B} & 0 \\ \boldsymbol{B}^T & 0 & \boldsymbol{a} \\ 0 & \boldsymbol{a}^T & 0 \end{bmatrix}, \boldsymbol{F} = \begin{bmatrix} \boldsymbol{C} \\ 0 \\ 0 \end{bmatrix},$$

$$\boldsymbol{A} = A_{ij} := a_h(\phi_i,\phi_j) + a_h^{\alpha}(\phi_i,\phi_j) \quad i,j \in \{1,\dots,N\},$$
$$\boldsymbol{B} = B_{ij} := b_h(\phi_i,\psi_j) \quad i \in \{1,\dots,M\} \; j \in \{1,\dots,N\},$$
$$\boldsymbol{C} = C_j := l_h(\phi_j) \quad j \in \{1,\dots,N\},$$

and $\boldsymbol{a}$ is the vector of element areas.

2.2 Virtual Element Projection $\Pi_E^0 \nabla v$

Based on the works of Gain et al. 2013; Veiga et al. 2014 and Chi et al. 2017, we consider the lower-order element (i.e., $k = 1, n_{p_k} = 3$ and $n_{p_{k-1}} = 2$) in which the set of basis functions for $P_k(E)$, (linear polynomial space): $m_\alpha^{(k)}, \alpha = 1,\dots, n_{p_k}$ is defined as

$$m_1^{(1)} = 1, \; m_2^{(1)} = \frac{x - x_C}{h_E}, m_3^{(1)} = \frac{y - y_C}{h_E}, \tag{6}$$

the gradients of $P_k(E)$ are

$$\nabla m_1^{(1)} = \begin{bmatrix} 0 \\ 0 \end{bmatrix}, \nabla m_2^{(1)} = \frac{1}{h_E}\begin{bmatrix} 1 \\ 0 \end{bmatrix}, \nabla m_3^{(1)} = \frac{1}{h_E}\begin{bmatrix} 0 \\ 1 \end{bmatrix}, \tag{7}$$

and the basis functions $\boldsymbol{m}_\alpha^{(k-1)}$, for the two-dimensional vector polynomial space $[P_{k-1}(E)]^2$, with $\alpha = 1,\dots, n_{p_{k-1}}$, are defined as

$$\boldsymbol{m}_1^{(0)} = \begin{bmatrix} 1 \\ 0 \end{bmatrix} \quad \text{and} \quad \boldsymbol{m}_2^{(0)} = \begin{bmatrix} 0 \\ 1 \end{bmatrix}, \tag{8}$$

where x_c and y_c are the coordinates of the centroid of the element E, $|E|$ is the element area, and $h_E = |E|^{1/2}$ is the average element size.
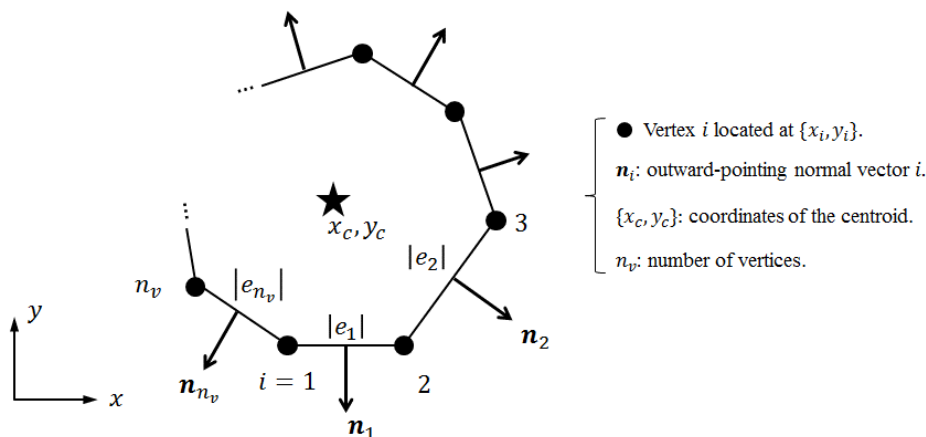
Figure 1: Local VEM spaces and degrees of freedom of a given element.

The first projection operator $\Pi_E^0 \nabla v$, which projects the gradient of v onto $[P_{k-1}(E)]^2$, satisfies the following expression:

$$\int_E \Pi_E^0 \nabla v . \boldsymbol{p} d\boldsymbol{x} = \int_E \nabla v . \boldsymbol{p} d\boldsymbol{x} = \oint_{\partial E} v . \boldsymbol{p} . \boldsymbol{n} ds - \int_E v \, \nabla . \boldsymbol{p} d\boldsymbol{x} \quad \forall \boldsymbol{p} \in [P_{k-1}(E)]^2 \qquad (9)$$

Introducing a set of shape functions for the local VEM space $V_h(E)$, $\phi_i(x), i = 1, \dots, n_v$, we can express $\Pi_E^0 \nabla v$ as

$$\Pi_E^0 \nabla v = \sum_{i=1}^{n_v} \Pi_E^0 \nabla \phi_i(\boldsymbol{x}) \, V_i \, .$$

Therefore, Eq. (9) can be rewritten as

$$\int_E \Pi_E^0 \nabla \phi_i . \boldsymbol{m}_\alpha^{(k-1)} d\boldsymbol{x} = \int_E \nabla \phi_i . \boldsymbol{m}_\alpha^{(k-1)} d\boldsymbol{x} = \oint_{\partial E} \phi_i . \boldsymbol{m}_\alpha^{(k-1)} . \boldsymbol{n} ds - \int_E \phi_i \nabla . \boldsymbol{m}_\alpha^{(k-1)} d\boldsymbol{x} \qquad (10)$$

We can also express $\Pi_E^0 \nabla \phi_i$ using the set of basis $\boldsymbol{m}_\alpha^{(k-1)}$ for $[P_{k-1}(E)]^2$ as

$$\Pi_E^0 \nabla \phi_i(\boldsymbol{x}) = \sum_{\beta=1}^{n_{p_{k-1}}} S_{i\beta} \, \boldsymbol{m}_\beta^{(k-1)}(\boldsymbol{x}) \, . \qquad (11)$$

Finally, Eq. (10) can be rewritten as

$$\sum_{\beta=1}^{n_{p_{k-1}}} S_{i\beta} \int_E \boldsymbol{m}_\beta^{(k-1)} . \boldsymbol{m}_\alpha^{(k-1)} \, d\boldsymbol{x} = \oint_{\partial E} \phi_i . \boldsymbol{m}_\alpha^{(k-1)} . \boldsymbol{n} ds - \int_E \phi_i \nabla . \boldsymbol{m}_\alpha^{(k-1)} d\boldsymbol{x} \qquad (12)$$

From Eq. (12), we can form the matrices $\boldsymbol{M}$ and $\boldsymbol{R}$ and compute the matrix $\boldsymbol{S}$ as

$$\boldsymbol{S} = \boldsymbol{R} \boldsymbol{M}^{-1} \qquad (13)$$

2.3 Virtual Element Projection $\Pi_E^\nabla v$

The second projection operator $\nabla \Pi_E^\nabla v$, projects v onto $P_k(E)$, as

$$\int_E \nabla \Pi_E^\nabla v . \nabla p d\boldsymbol{x} = \int_E \nabla v . \nabla p d\boldsymbol{x} = \oint_{\partial E} v \nabla p . \boldsymbol{n} ds - \int_E v \Delta p d\boldsymbol{x} \quad \forall p \epsilon P_k(E) . \tag{14}$$

We express $\Pi_E^\nabla v$ using the shape functions ϕ_i as

$$\Pi_E^\nabla v = \sum_{i=1}^{n_v} \Pi_E^\nabla \phi_i(\boldsymbol{x}) V_i .$$

Therefore, Eq. (14) can be rewritten as

$$\int_E \nabla \Pi_E^\nabla \phi_i . \nabla m_\alpha^{(k)} d\boldsymbol{x} = \int_E \nabla \phi_i . \nabla m_\alpha^{(k)} d\boldsymbol{x} = \oint_{\partial E} \phi_i \nabla m_\alpha^{(k)} . \boldsymbol{n} ds - \int_E \phi_i \Delta m_\alpha^{(k)} d\boldsymbol{x} \tag{15}$$

We can also express $\Pi_E^\nabla \phi_i$ in terms of the set of basis $m_\alpha^{(k)}$ for $P_k(E)$ as:

$$\Pi_E^\nabla \phi_i = \sum_{\alpha=1}^{n_{pk}} S_{i\alpha}^\nabla m_\alpha^{(k)} . \tag{16}$$

Combining Eqs. (15) and (16) we obtain

$$\sum_{\beta=2}^{n_{pk}} S_{i\beta}^\nabla \int_E \nabla m_\beta^{(k)} . \nabla m_\alpha^{(k)} d\boldsymbol{x} = \oint_{\partial E} \phi_i \nabla m_\alpha^{(k)} . \boldsymbol{n} ds - \int_E \phi_i \Delta m_\alpha^{(k)} d\boldsymbol{x} \tag{17}$$

From Eq. (17), we can form matrices $\boldsymbol{M^\nabla}$ and $\boldsymbol{R^\nabla}$ and compute the matrix $\boldsymbol{S^\nabla}$ as

$$\boldsymbol{S^\nabla} = \boldsymbol{R^\nabla} \boldsymbol{M^{\nabla^{-1}}} \tag{18}$$

Additionally, we can express $\Pi_E^\nabla \phi_i(\boldsymbol{x})$ in terms of the shape funtions ϕ_i as

$$\Pi_E^\nabla \phi_i(\boldsymbol{x}) = \sum_{i=1}^{n_v} P_{ij}^\nabla \phi_j(\boldsymbol{x}) \tag{19}$$

Using Eq. (4), we can express the terms a_h, a_h^α and b_h as follows:

Computing a_h:

We introduce the discrete counterpart $a_h^E : \boldsymbol{V}_h^E \times \boldsymbol{V}_h^E \to \mathbb{R}$ of a^E as

$$a_h^E(\boldsymbol{u}_h, \boldsymbol{v}_h) := (\Pi_E^0 \nabla \boldsymbol{u}_h, \Pi_E^0 \nabla \boldsymbol{v}_h)_{0,E} + S^E(\boldsymbol{u}_h - \Pi_E^\nabla \boldsymbol{u}_h, \boldsymbol{v}_h - \Pi_E^\nabla \boldsymbol{v}_h) \tag{20}$$

and, we define

$$a_h(\boldsymbol{u}_h, \boldsymbol{v}_h) := \sum_{E \in \Omega_h} a_h^E(\boldsymbol{u}_h, \boldsymbol{v}_h)$$

to be the discrete counterpart of a. Therefore

$$a_h^E(\phi_i, \phi_j) = \int_E \Pi_E^0 \nabla \phi_i \cdot \Pi_E^0 \nabla \phi_j dx + S(\phi_i - \Pi_E^\nabla \phi_i, \phi_j - \Pi_E^\nabla \phi_j) \tag{21}$$

Substituting Eq. (11) into Eq. (21), the consistency term can be expressed as

$$\int_E \Pi_E^0 \nabla \phi_i \cdot \Pi_E^0 \nabla \phi_j dx = \sum_{\alpha=1}^{n_{p_{k-1}}} \sum_{\beta=1}^{n_{p_{k-1}}} S_{i\alpha} S_{j\beta} \int_E \boldsymbol{m}_\beta^{(k-1)} \cdot \boldsymbol{m}_\alpha^{(k-1)} dx = \boldsymbol{SMS}^T, \tag{22}$$

and substituting Eq. (19) into Eq. (21), the stability term is given by

$$S(\phi_i - \Pi_E^\nabla \phi_i, \phi_j - \Pi_E^\nabla \phi_j) = (\delta_{ik} - P_{ik}^\nabla)(\delta_{jk} - P_{jk}^\nabla) = (\boldsymbol{I} - \boldsymbol{P}^\nabla)(\boldsymbol{I} - \boldsymbol{P}^\nabla)^T, \tag{23}$$

Computing a_h^α:

The discrete counterpart of a_α is

$$a_h^{\alpha E}(\phi_i, \phi_j) = \bar{\alpha} \int_E \Pi_E^\nabla \phi_i \cdot \Pi_E^\nabla \phi_j dx, \tag{24}$$

and, substituting Eq. (16) into Eq. (24), we obtain

$$\bar{\alpha} \int_E \Pi_E^\nabla \phi_i \cdot \Pi_E^\nabla \phi_j dx = \bar{\alpha} \sum_{\alpha=1}^{n_{p_k}} \sum_{\beta=1}^{n_{p_k}} S_{i\alpha}^\nabla S_{i\beta}^\nabla \int_E m_\beta^{(k)} \cdot m_\alpha^{(k)} dx = \bar{\alpha} |E| \boldsymbol{NN}^T, \tag{25}$$

where

$$\boldsymbol{N} = \begin{bmatrix} S_{11}^\nabla & S_{12}^\nabla & S_{13}^\nabla \\ S_{21}^\nabla & S_{22}^\nabla & S_2^\nabla \\ \vdots & \vdots & \vdots \\ S_{n_v 1}^\nabla & S_{n_v 2}^\nabla & S_{n_v 3}^\nabla \end{bmatrix} \begin{bmatrix} m_1^{(1)}(\boldsymbol{x}_c) \\ m_2^{(1)}(\boldsymbol{x}_c) \\ m_3^{(1)}(\boldsymbol{x}_c) \end{bmatrix} \quad \text{and} \quad \boldsymbol{x}_c = [x_c \, y_c]$$

Computing b_h:

Substituting Eq. (16) into Eq. (26), the discrete counterpart of b can be expressed as

$$b_h^E(\phi_i) = -\int_E \nabla . \Pi_E^\nabla \phi_i \, dx = -\sum_{\alpha=1}^{n_{p_k}} S_{i\alpha}^\nabla \nabla m_\alpha^{(k)} \tag{26}$$

or

$$b_h^E = -\begin{bmatrix} S_{11}^\nabla & S_{12}^\nabla & S_{13}^\nabla \\ S_{21}^\nabla & S_{22}^\nabla & S_2^\nabla \\ \vdots & \vdots & \vdots \\ S_{n_v 1}^\nabla & S_{n_v 2}^\nabla & S_{n_v 3}^\nabla \end{bmatrix} \begin{bmatrix} \nabla m_1^{(1)} \\ \nabla m_2^{(1)} \\ \nabla m_3^{(1)} \end{bmatrix} = -\frac{1}{h_E} \begin{bmatrix} S_{12}^\nabla \\ S_{13}^\nabla \\ \vdots \\ S_{n_v 2}^\nabla \\ S_{n_v 2}^\nabla \end{bmatrix}, i = 1, \dots, n_v. \tag{27}$$

2.4 Time comparison VEM vs. FEM

To illustrate the use of the VEM method, consider the diffuser domain problem (Pereira et al. 2016). The geometry and boundary conditions are illustrated in Figure 2a. The other numerical values are the dynamic viscosity $\mu = 1$ and the density of the fluid $\rho = 1$. For the simulation, we used an Intel Core i7-8700 CPU @3.20GHz, with 16GB of RAM, and the Microsoft Windows 10

64-bit operating system. The numerical results of the velocity and pressure fields, using both VEM and FEM, are shown in Figures 2b and 2c, respectively.
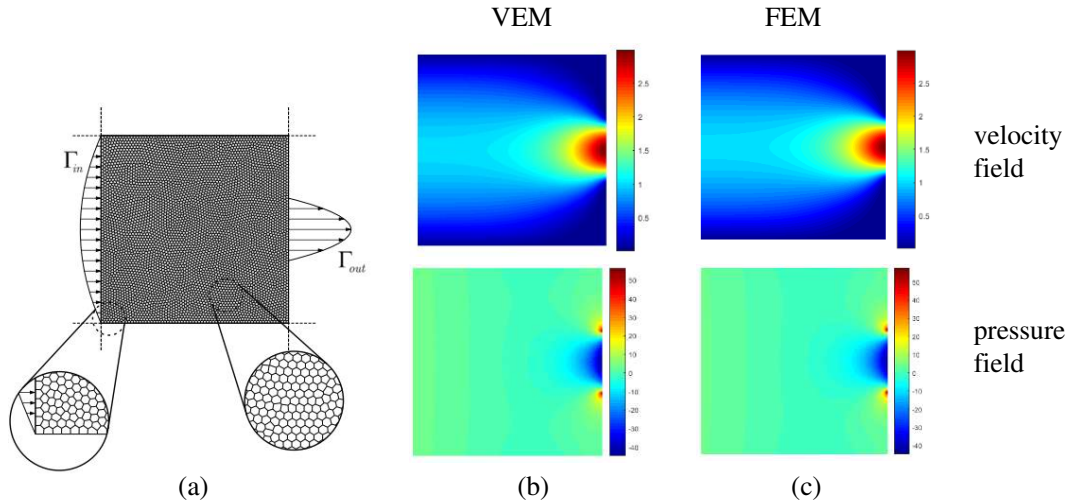
Figure 2: (a) Geometry and boundary condition of the diffuser square problem using polygonal elements, solution of the diffuser square problem using (b) VEM and (c) FEM method.

In our numerical tests, we computed the total velocity and the average pressure at the center of the domain, for different levels of polygonal mesh refinement using the FEM and the VEM. The results are shown in Figure 3a and 3b, respectively. It is noteworthy that the computational time with respect to the size of the problem increases faster in the FEM compared to the VEM (see Figure 3c).
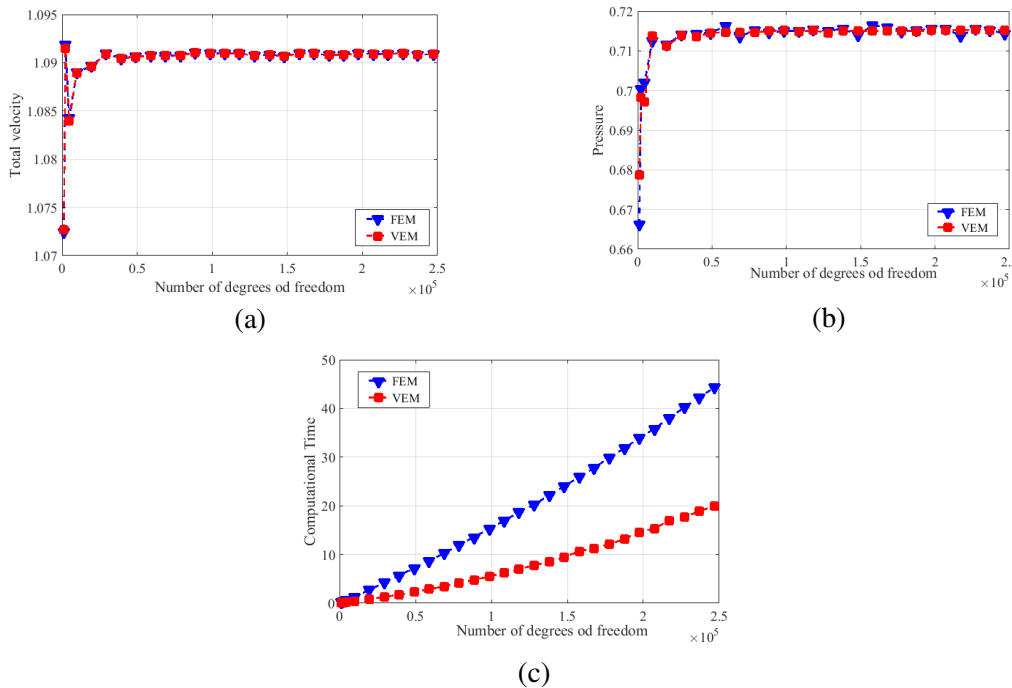
Figure 3: Convergence of the: (a) velocity value at the center of the domain; and (b) average value of the pressure at the center of the domain; (c) Computational time comparison between the FEM and VEM.

3 TOPOLOGY OPTIMIZATION

The objective and constraint functions, f and g respectively, of the optimization problem for the minimization of the dissipated power, neglecting the applied forces on the fluid, and subject to a constraint on its volume are given by

$$\min_{\rho} \quad f = \frac{1}{2}\mu \int_{\Omega} \nabla \boldsymbol{u} : \nabla \boldsymbol{u} \, d\Omega + \frac{1}{2} \int_{\Omega} \bar{\alpha}(\rho)\boldsymbol{u}.\boldsymbol{u} \, d\Omega$$

s.t.

$$g = \int_{\Omega} \rho d\Omega - V_s \leq 0 \tag{28}$$

with

$$a(\boldsymbol{u}, \boldsymbol{v}) + a_\alpha(\boldsymbol{u}, \boldsymbol{v}) + b(\boldsymbol{v}, p) = 0$$
$$b(\boldsymbol{u}, q) = 0$$

and $\quad 0 \leq \rho \leq 1$

The first term of the objective function f, corresponds to the dissipation owing to the viscous dissipative effects, while the second term corresponds to the dissipative effects of the porous media model, ρ (design variable) that represents the value of the pseudo-densities at each point of the domain; V_s is an upper bound for the final volume to be achieved in the solution of the optimization problem.
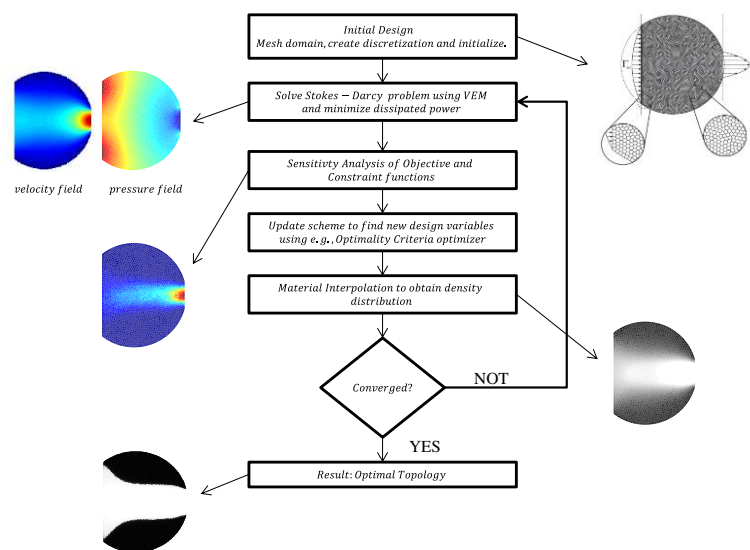
Figure 4: Flowchart for the optimal solution of the diffuser problem.

The Stokes–Darcy system of equations is used as a constraint in the topology optimization problem and is solved by the VEM. The Optimality Criteria, OC, (Gunwant and Misra, 2012) is used as the optimizer, and the objective and constraint function gradients, $\partial f/\partial \rho$ and $\partial g/\partial \rho$, respectively, are obtained analytically. The topology optimization code includes a simple and efficient implementation of the sensitivities and a straightforward integration with polygonal VEM codes (Pereira et al. 2016). The main steps of the topology optimization process are illustrated in the flowchart depicted in Figure 4.

4   NUMERICAL RESULTS

4.1   Diffuser problem

We present numerical examples for the minimization of the viscous drag in both typical domains (see Figures 5a and 6a) presented by Pereira et al. (2016). The viscosity of the fluid was $\mu = 1$ and we used continuation on the penalty parameter with values $q = \{0.01; 0.1; 1\}$. The OC algorithm is used as the optimizer with a maximum of 150 iterations.
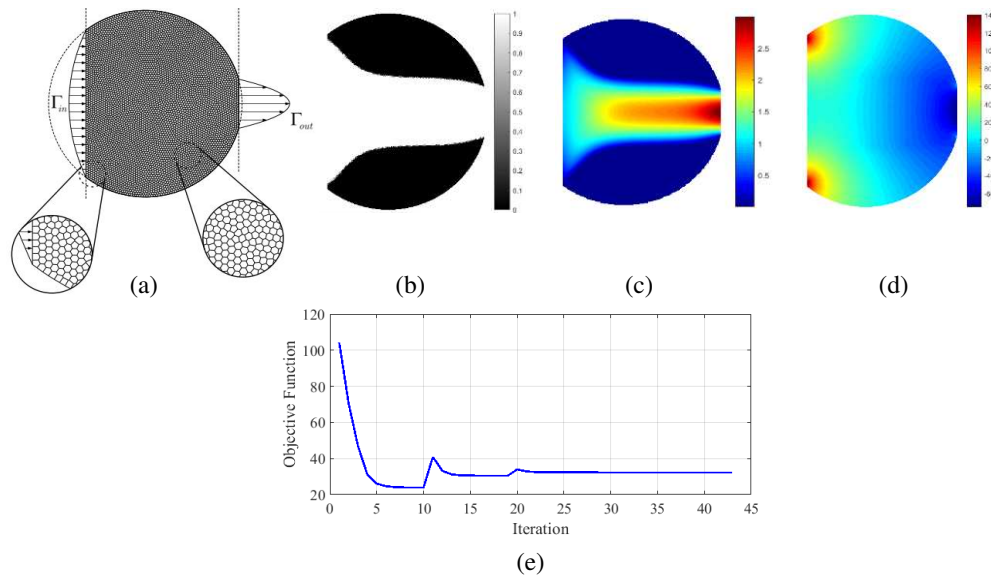
Figure 5: (a) Geometry and boundary conditions for the diffuser (non-Cartesian domain); (b) optimal topology; (c) velocity field; (d) pressure field; and (e) convergence history.
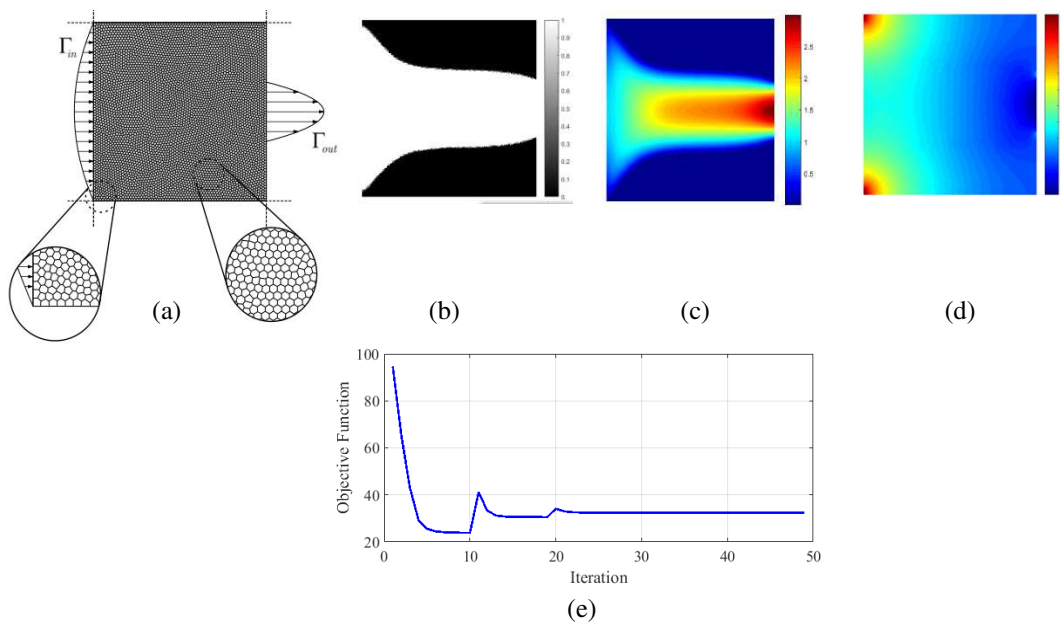
Figure 6: (a) Geometry and boundary conditions for the diffuser (Cartesian domain); (b) optimal topology; (c) velocity field; (d) pressure field; and (e) convergence history.

The solution for the curved domain was obtained for a volume fraction $V = 0.46085$ (see Figure 5b) to match the solution for the square domain, where $V = 0.5$ (see Figure 6b), as prescribed by Borrvall and Petersson, (2003), using 10,000 polygonal elements. The convergence histories of the objective function f, are shown in Figures 5e and 6e, respectively.

5   CONCLUSIONS

In this work we presented an application of topology optimization for fluid flow problems, governed by Stokes-Darcy equation, using the virtual element method (VEM). Representative examples found in the literature were tested and a comparative study was carried out between the FEM and VEM. We observed that the VEM presented a better computational performance and that this method is very well-suited to be used in topology optimization problems. An extension of the VEM for solving 3D fluid flow topology optimization problems, using the Navier-Stokes equations, is currently under investigation by the authors.

REFERENCES

Ahmad, B., Alsaedi, A., Brezzi, F., Marini, L.D., and Russo, A., Equivalent projectors for virtual element methods. *Computers and Mathematics with Applications*, 66(3), p.376–391, 2013. Available at: http://dx.doi.org/10.1016/j.camwa.2013.05.015.

Borrvall, T., and Petersson, J., Topology optimization of fluids in Stokes flow. *International Journal for Numerical Methods in Fluids*, 41, p.77–107, 2003. (doi: 10.1002/fld.426)

Brenner, S.C., Guan, Q., and Sung, L., Some Estimates for Virtual Element Methods. , 17(4), p.553–574, 2017. (doi:10.1515/cmam-2017-0008).

Chi, H., Veiga, L.B., and Paulino, G.H., Some basic formulations of the virtual element method (VEM) for finite deformations. *Comput. Methods Appl. Mech. Engrg.*, 318, p.148–192, 2017. (doi:10.1016/j.cma.2016.12.020).

Gain, A.L., Talischi, C., and Paulino, G.H., *On the Virtual Element Method for Three-Dimensional Elasticity Problems on Arbitrary Polyhedral Meshes*, Urbana-Champaign, USA, 2013.

Gartling, D.K., Hickox, C.E., and Givler, R.C., Simulation of Coupled Viscous and Porous Flow Problems. *International Journal of Computationa Fluid Dynamics*, 7, p.23–48, 2007. (doi: 10.1080/10618569608940751).

Gunwant, D., and Misra, A., Topology Optimization of Continuum Structures using Optimality Criterion Approach in Ansys. *International Journal of Advances in Engineering & Technology*, 5(1), p.470–485, 2012.

Pereira, A., Talischi, C., Paulino, G.H., Menezes, I.F.M., and Carvalho, M.S., Fluid flow topology optimization in PolyTop : stability and computational implementation. *Structural and Multidisciplinary Optimization*, 54, p.1345–1364, 2016.

Sutton, O.J., The virtual element method in 50 lines of Matlab. *Numerical Algorithms*, 75(4), p.1141–1159, 2017. (doi: 10.1007/s11075-016-0235-3).

Veiga, L.B., Brezzi, F., and Cangiani, A., Basic Principles of Virtual Element Methods. *Mathematical Models and Methods in Applied Sciences*, 23(1), p.199–214, 2013. (doi: 10.1142/S0218202512500492).

Veiga, L.B., Brezzi, F., Marini, L.D., and Russo, A., The Hitchhiker's Guide to the Virtual Element Method. *Mathematical Models and Methods in Applied Sciences*, 24(8), 2014.